Contents lists available at ScienceDirect

Ultramicroscopy

Bragg holography of nano-crystals

Tatiana Latychevskaia [a,*], Cathal Cassidy [b], Tsumoru Shintake [b]

[a] *Paul Scherrer Institute, Forschungsstrasse 111, 5232 Villigen, Switzerland*
[b] *Quantum wave microscopy unit, Okinawa Institute of Science and Technology, 1919-1, Tancha, Onna, Kunigami District, Okinawa 904-0495, Japan*

ARTICLE INFO

ABSTRACT

Crystal diffraction is a well-established technique for high-resolution structural analysis of material science and biological samples. However, the recovered structure is a result of averaging over all the unit cells in the crystal, which smears out the imperfections, atomic defects, or asymmetries and chiral properties of the individual molecules. We propose Bragg holography, where a nano-crystal is imaged at a defocus distance allowing separation of the diffracted beams, without turning them into peaks. The presence of a reference wave gives rise to a Bragg hologram, which can be reconstructed by conventional holographic reconstruction algorithms. The recovered complex-valued wavefront contains the complete information about the atomic distribution in the crystal, including defects. Bragg holography is demonstrated for gold nano-crystals, and its feasibility for biological nano-crystals is shown.

1. Introduction

X-ray crystallography, where signal is averaged over thousands of unit cells, has been routinely applied for solving the molecular structure of biological and material science samples [1]. The current trends in electron crystallography are aimed towards analysis of nano-crystals, specifically their structure and deformations at atomic scale [2–4]. High-resolution imaging of material science and biological crystalline samples can be realized in an electron microscope by a number of established techniques, such as selected-area electron diffraction (SAED) and high-resolution transmission electron microscopy (HRTEM). Standard SAED yields data with good signal-to-noise ratio (SNR) and insensitivity to real space specimen drift; but this technique yields only structure factor amplitudes, and the corresponding phases must be obtained via other means, such as molecular replacement [5]. Conventional HRTEM yields a real-space intensity image which, as is well-known, is greatly corrupted by the optical transfer (signal at some frequencies has inverted contrast, and signal at other frequencies is lost completely). Thus, white dots in the image may not actually be at the atomic positions at all. There are other strategies to address these challenges. In 1992, Coene et al. demonstrated the unambiguous high-resolution reconstruction of samples obtained from a focal series acquired in a transmission electron microscope (TEM), which has become a practical tool for image analysis in HRTEM [6]. Coherent diffraction imaging (CDI) [7] has been demonstrated in TEM by Zuo et al. who retrieved the structure of a double-walled carbon nanotube at atomic resolution from a diffraction pattern acquired using TEM with a nominal

microscope point resolution of 2.2 Å [8]. CDI can be successfully used for reconstruction of crystalline nano-particles in combination with other techniques [2,9,10]. However, CDI of crystalline samples is highly challenging because of non-uniqueness of the reconstructed sample structure [11]. Recently Russo and Henderson suggested imaging nanocrystals in defocus mode and demonstrated that this creates a set of Bragg diffracted waves that appear separately from one another [12].

In this study we show how unambiguous crystal structure can be recovered from a single image in a TEM, by utilizing a Bragg hologram. The acquisition configuration is such that we are able to acquire the genuine amplitude and phase of the specimen transmitted wave, without any associated reversals or losses at specific frequencies. Having access to the full wave allows numerical back-propagation to the specimen, with confidence that the reconstructed image signal can be directly related to the sample structure (including defects). Further to that, in principle we can also propagate to any arbitrary plane within the three-dimensional specimen. The details, including some practical limitations and constraints, are the subject of this paper.

2. Results

2.1. Principle

Fig. 1 shows a schematic diagram of beam propagation in the electron microscope for Bragg holography. A nano-crystal illuminated with

---
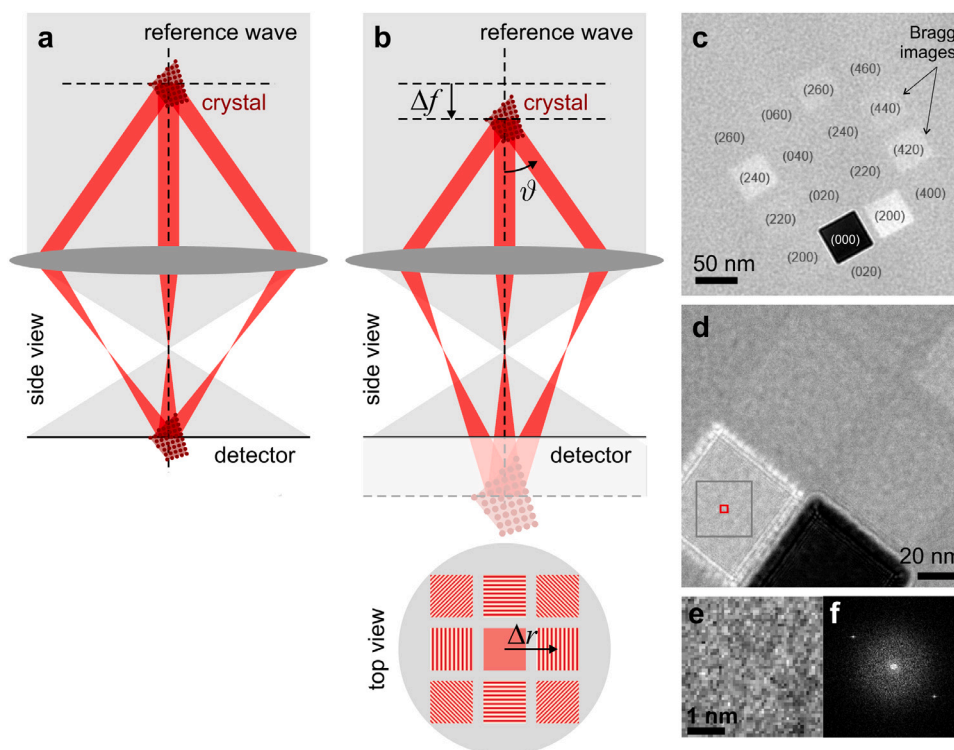
Fig. 1. Bragg holography of nano-crystals. Schematic diagram of beam propagation in an electron microscope, when nano-crystal is imaged (a) in-focus (a) and (b) at a defocus Δf, ϑ is the diffraction angle. The first-order Bragg diffracted waves are observed at $\vartheta = 2\vartheta_{\mathrm{B}}$. The interference patterns formed by superposition with the reference wave (Bragg images) are shown in top view in (b). (c) Example of an experimental Bragg hologram of MgO nano-crystal acquired with 300 keV electrons at defocus distance of 7 μm. At this magnification with the utilized experimental hardware, the pixel size was insufficient to sample the fringes inside each Bragg image. (d) A Bragg hologram acquired at a higher magnification, the interference pattern in the red square is shown in (e), exhibiting periodical fringes. (f) Amplitude of Fourier transform of the interference pattern in the gray square in (d), showing two side-peaks due to periodic fringes in the interference pattern. (For interpretation of the references to color in this figure legend, the reader is referred to the web version of this article.)

a plane electron wave diffracts the electron wave at angles governed by Bragg's law

$$2d \sin \vartheta_{\mathrm{B}} = \lambda n, \tag{1}$$

where ϑ_{B} is the diffraction angle, λ is the wavelength, n is an integer, d is the distance between the diffracting planes. An in-focus image of the nano-crystal can be obtained by using a system of lenses which focuses all the diffracted waves back together into an image (Fig. 1(a)). When the nano-crystal is imaged at defocus (Fig. 1(b)), the Bragg diffracted waves appear separated from one another, laterally positioned at a distance

$$\Delta r = \Delta f \tan (2\vartheta_{\mathrm{B}}) \tag{2}$$

from the zero-order image, Fig. 1(c)–(f), where Δf is the defocus. An example of the defocus series is shown in Fig. 2. A Bragg hologram is a defocused image of a crystal illuminated with a plane wave with an extent that significantly exceeds the lateral size of the crystal, so that the diffracted beams interfere with the illuminating plane wave, forming holograms. The complete information about the complex-valued distribution of the scattered waves is thereby recorded according to the holography principle [13], as shown in Fig. 1(a)–(b). We refer to these individual interference patterns as Bragg images, and the full interference pattern that includes all Bragg images as a Bragg hologram. The reference wave extent should be broad enough to cover all the diffraction orders. The resulting Bragg hologram has components of both in-line and off axis holograms. In the zero-diffraction order, an in-line hologram is formed by interference with the wave propagating through the crystal. In the higher diffraction orders, the diffracted beams interfere with the unperturbed reference beam, thus creating off-axis holograms (Fig. 1(c)–(f)). The number of Bragg images and the symmetry of their positions relative to the center of the Bragg hologram

(unlike the 2D hologram distribution) are given by the intersection of the allowed diffraction orders with the Ewald sphere, as shown in Fig. 3.

A Bragg hologram can be reconstructed by applying conventional holographic reconstruction algorithms. The signal in the central spot is an in-line hologram distribution, and this type of hologram is known to suffer from the so-called twin-image [14,15] — an out-of-focus sample image superimposed onto an in-focus image. As we show below, in both cases of non-biological and for biological nano-crystals this problem can be solved and the complex-valued distribution of the exit wave, that is the wavefront right behind the sample, can be reconstructed and contains the complete 3D structural information about the sample.

2.2. Non-biological crystals

For non-biological crystals, the twin image problem can be solved by numerically removing the signal in the central region (zero-order Bragg image) and replacing it with a constant value equal to the background (intensity of the reference wave), as described in Appendix B: Bragg hologram high-pass filtering. To achieve separation between the zero-order and higher-order Bragg images, the lateral size of the crystal s should be smaller than the center of the first-order Bragg image:

$$s < \Delta f \tan (2\vartheta_{\mathrm{B}}). \tag{3}$$

The numerically filtered Bragg hologram is then reconstructed by propagating the wavefront from the defocus plane to the in-focus plane. The wavefront propagation is calculated by the angular spectrum (ASM) method [16–18], which boils down to computing the exit wave wavefront distribution u from the wavefront u_{B} in the Bragg hologram plane by applying the following transform:

$$u = \mathrm{FT}^{-1} \left\{ \mathrm{FT}(u_{\mathrm{B}}) \exp \left[\frac{i 2\pi z}{\lambda} \sqrt{1 - (\lambda f_x)^2 - (\lambda f_y)^2} \right] \right\}, \tag{4}$$
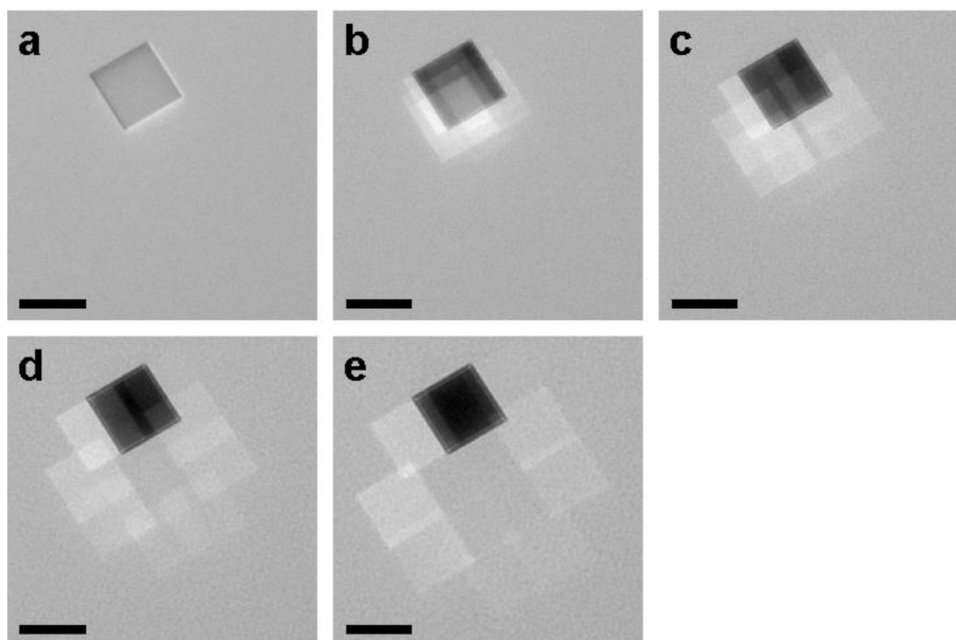
Fig. 2. Bragg images as function of defocus distance for a MgO nano-crystal of about 50 nm × 50 nm × 50 nm in size, close to (200) orientation, measured with 300 keV electrons at: (a) close to focus, (b) +1 μm, (c) +2 μm, (d) +3 μm, and (e) +4 μm defocus. Bragg images appear at a distance Δr from the center of the Bragg hologram, where Δr is defined by Eq. (2). For (200) MgO nano-crystals, the distance between atomic planes is 2.11 Å which gives for 300 keV electrons the Bragg diffraction angle of $\vartheta_B = 4.67$ mrad. At defocus of $\Delta f = +4$ μm (not shown here), the positions of the Bragg images are $\Delta r = 50$ nm from the center, so that the Bragg images would be separated from the central shadow image. At this magnification with the utilized experimental hardware, the pixel size was insufficient to sample the fringes inside each Bragg image. The scalebars correspond to 50 nm. The intensity range is the same for all the panels.

where FT and FT^{-1} are Fourier and inverse Fourier transforms, respectively, (f_x, f_y) are the coordinates in the Fourier plane, and z is the distance between the two planes. By setting $z = \Delta f$, the complex-valued wavefront distribution right behind the sample is obtained. By setting z to $z = \Delta f + \Delta z$ the complex-valued wavefront distribution at a distance Δz into the sample is obtained. Thus, by selecting Δz values, in principle, a 3D distribution of the wavefronts at different planes inside the sample can be obtained. However, it must be noted that in order to resolve the atomic arrangements along the z-axis, z-resolution, defined by the extent of the Bragg hologram (numerical aperture), must be sufficiently high. The central region in the Bragg hologram (zero-order Bragg image) contains the information related to a uniform, constant distribution. Setting the zero-order Bragg image to the background intensity during the reconstruction procedure is equivalent to subtraction of that constant. Since the atomic distribution is described by a non-constant and typically a periodical function (except for defects), this constant off-set can be ignored. In the next sub-section we show an example of reconstructed spatial distribution of atoms and a defect obtained by this approach.

2.2.1. Simulated Bragg hologram

A simulated example of Bragg hologram of a model crystal and its reconstruction are shown in Fig. 4. The model crystal is made of finite-sized hexagonal (graphene-like) lattices in three planes. In the middle plane, one node (atom) is missing, as shown in Fig. 4(a)–(c). The corresponding Bragg hologram was obtained by calculating wavefront propagation through the three planes and then to a defocus distance. The transmission function of each layer is given by $\exp[i\sigma v_z(x, y)]$, where σ is the interaction parameter and $v_z(x, y)$ is the projected potential, each layer was assumed to be a hexagonal-arranged lattice of carbon atoms with the closest distance between the atom of 1.42 Å, the distance between the planes was 3.35 Å, the electron energy was 80 keV. The defocus distance was selected such that the individual Bragg images are separated from one another, $\Delta f = 500$ nm, shown in Fig. 4(d). In the obtained Bragg hologram the zero-order Bragg image was replaced by a constant (Fig. 4(e)). The crystal distribution was

reconstructed by calculating the wavefront propagation from the plane of the Bragg hologram to the three planes inside the sample using the ASM. The ASM allows wavefront propagation to any plane inside the sample, which allows quasi three-dimensional reconstruction. The corresponding reconstructed distributions are shown in Fig. 4(g)–(i). It is apparent, in this case, that the reconstructed distributions are almost indistinguishable, and the missing atom in plane 2 cannot be seen. The reason is that the axial resolution $R_z = 2\lambda/(NA)^2$ [19], where NA is the numerical aperture NA $= S/(2z)$ where S is the detector size and z is the sample-to-detector distance, amounts to $R_z = 1.3$ nm, which is much larger then the distance between the planes, and the signal from the adjacent planes are practically appear in one plane. Thus, although three-dimensional information is reconstructed, it cannot be resolved due to poor axial resolution. When the distance between the planes exceeds the resolution limit, the signal from different planes can be distinguished, as shown in Fig. 4(j)–(l), where the missing atom is reconstructed in plane 2. The results shown in Fig. 4 demonstrate that the filtering out of the low-resolution information allows artifact-free recovery of the high-resolution information, so that the individual defect could be accurately retrieved. The limiting factor remains the axial resolution, which can be improved by either adjusting the geometrical parameters of the setup, or by using advanced reconstruction methods that allow separation of the signal from different planes along z-axis [20]. Aside from the black dots which represent the actual atoms, there is some background texture (lines and flower-like features) in the reconstructions shown in Fig. 4(j)–(l). This relates to the interference of the waves from the out-of-focus atoms from adjacent planes.

2.2.2. Experimental Bragg hologram

Experimental results obtained by Bragg holography are shown in Fig. 5. The details of electron diffraction experiments are provided in Appendix A. As test samples we used MgO and gold nano-crystals. An image of a gold nano-crystal acquired at close to focus conditions is shown in Fig. 5(a). A Bragg hologram of the same crystal is shown in Fig. 5(b), and the same hologram with the numerically filtered
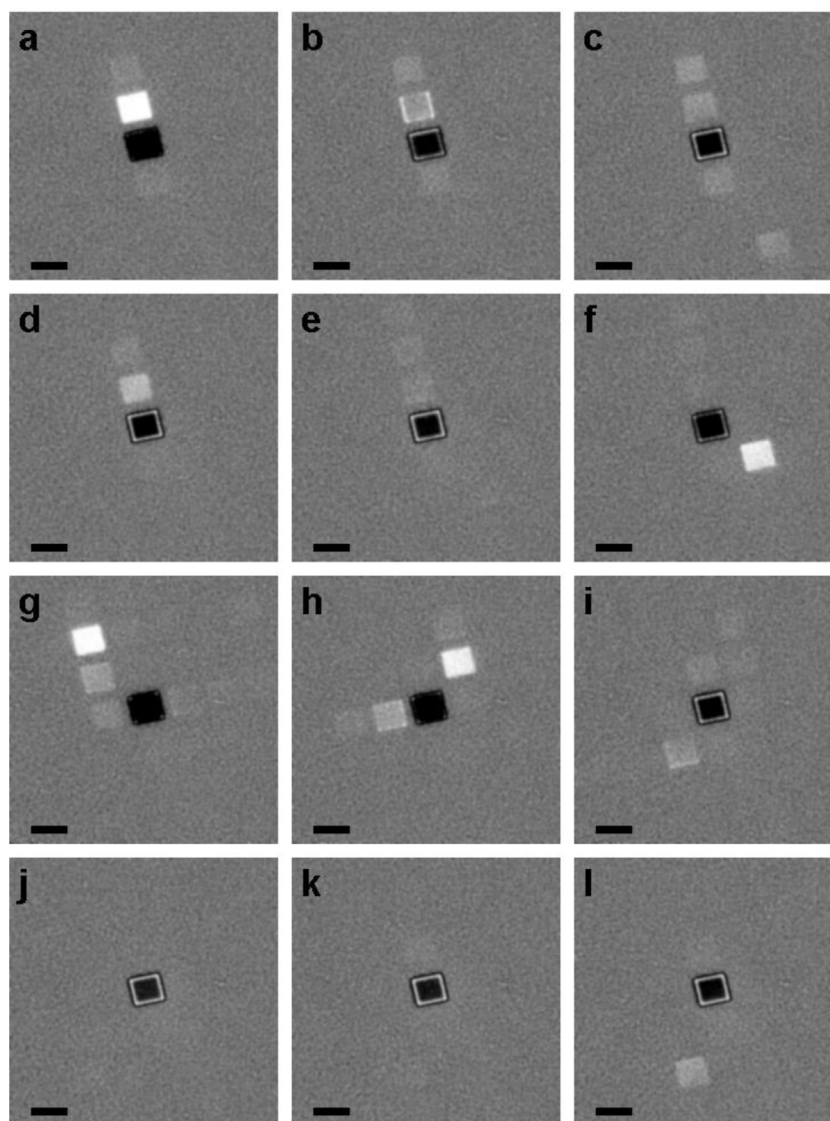
Fig. 3. Bragg images of MgO crystal of about 50 nm × 50 nm × 50 nm in size, close to (200) orientation, acquired at defocus of +5 μm, when the sample was tilted in 1° increments, from (a) −6° to (l) +5°. The image is zoomed out to show the distribution of the Bragg images as a function of tilt; the sampling at this magnification is insufficient to resolve the interference patterns inside each Bragg image. The scalebars correspond to 50 nm. The intensity range is the same for all the panels. The axis of rotation corresponds to the vertical direction in the shown micrographs.

zero-order Bragg image is shown in Fig. 5(c), the details of numerical filtering are provided in Appendix B: Bragg hologram high-pass filtering. The complex-valued exit wave reconstructed from the Bragg hologram is shown in Fig. 5(d) and (e). Artifact-free reconstruction is obtained from the filtered Bragg hologram, where the zero-order diffracted wave in the center of the hologram is set to zero (Fig. 5(e) and (f)). Atomic planes can be resolved in the obtained reconstructions (Fig. 5(f) and (g)). From the results shown in Fig. 5 it is evident that while conventional imaging provides intensity measurement only (Fig. 5(a)), the Bragg hologram captures the amplitude and phase distributions of the scattered wavefront (Fig. 5(f) and (g)).

2.3. Biological crystals

A particularly interesting application of Bragg holography is in imaging of biological nano-crystals. The lattice constant in biological crystals is an order of magnitude larger than that in material science nano-crystals and therefore the Bragg diffraction angles are respectively smaller. This in turn causes an experimental difficulty to detect the Bragg images separately from the central shadow and from each

other, as much larger defocus distances are needed. For example, for a 30 nm bacteriorhodopsin 2D crystal with trimer-to-trimer distance of 6.3 nm and the distance between the diffracting planes of 5.4 nm (Fig. 6(a)–(b)), imaged with electrons of 300 keV kinetic energy, a defocus distance of approximately 83 μm would be required to get the center of the first-order Bragg image separated from the central Bragg image. Moreover, at such large defocus distances, the Fresnel diffraction effects are substantial, resulting in each Bragg image being not localized to a certain region but spread over the entire Bragg hologram area and overlapping with other Bragg images, the effect of which cannot be avoided or numerically filtered. On the other hand, the twin image signal becomes less disturbing at large defocus distances close to Fraunhofer holography regime [21], because the waves diffracted by the individual atoms are diffracted at high angles given by $\propto \lambda/a$, where a is typical inter-atomic distance. In this case, there is no need for filtering out the central Bragg image and the entire Bragg hologram can be numerically processed, an example is shown in Fig. 6(c)–(f). At smaller, and more realistic defocus distances, such as 10 μm, it is possible to retrieve the nano-crystal structure from its Bragg hologram, although the twin image is present as a low-frequency
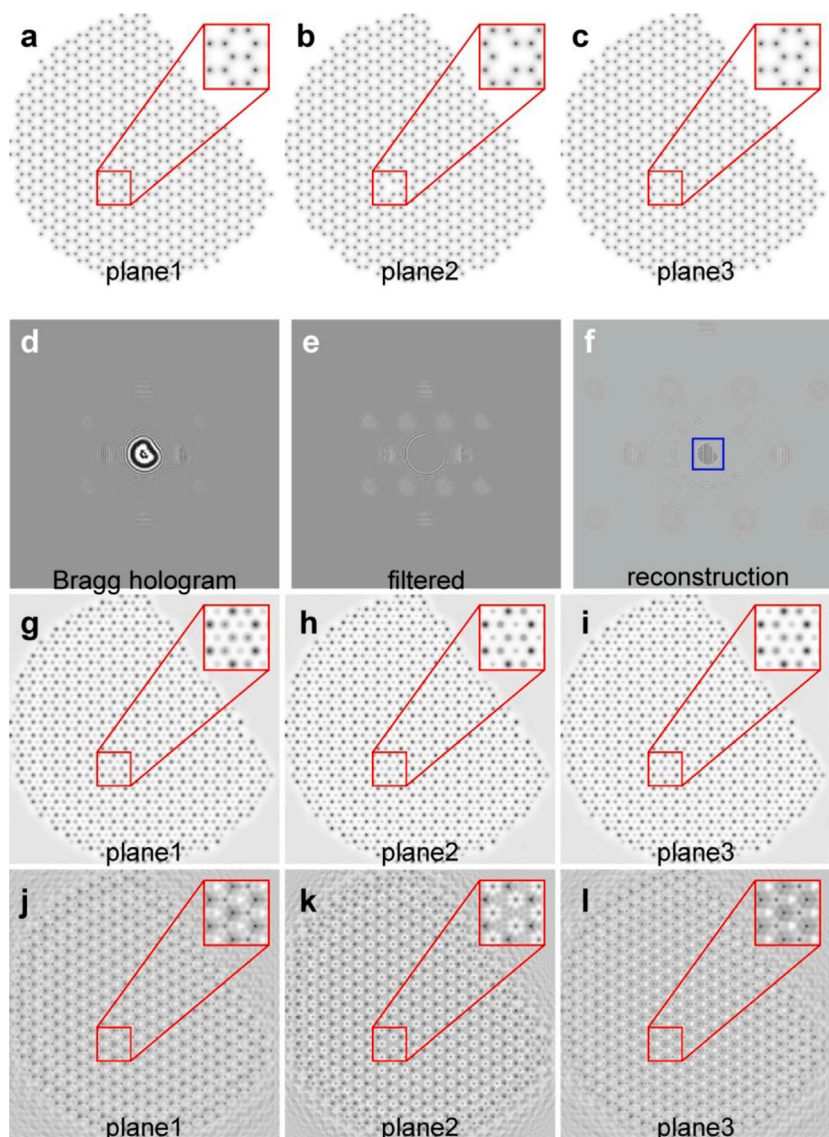
Fig. 4. Illustration for imaging of individual defects by Bragg holography. (a)–(c) A 3D crystal consisting of three planes with a single defect in the middle plane (plane2), the defect is in the region shown in the red square. (d) The corresponding Bragg hologram. (e) Filtered Bragg hologram, where the zero-order Bragg image is replaced by a constant. (f) Exit wave-front distribution reconstructed from the Bragg hologram, phase distribution is shown. (g)–(i) Reconstructed phase distributions at the three planes in the sample; the distance between the planes is 3.35 Å. (j)–(l) Reconstructed phase distributions at the three planes in the sample; the distance between the planes is 20 nm. The black dots represent the actual atoms, and are the features of primary interest in the current work. The background texture in the reconstructions (with lines and flower-like patterns) arise from the numerical reconstruction process, and relates to the interference of the waves from the out-of-focus atoms from adjacent planes. (For interpretation of the references to color in this figure legend, the reader is referred to the web version of this article.)

background signal Fig. 6(e)–(f) (details of the simulations are provided in Appendix C: Simulation of Bragg hologram of bacteriorhodopsin). Because the zero-order Bragg image does not need to be filtered out, the zero-order and the first-order Bragg images do not need to be clearly separated. For this reason, the restriction on the crystal size given by Eq. (3) does not apply for biological crystals.

The radiation dose for high-resolution biological imaging amounts to about 5 $e/\text{Å}^2$ to preserve the atomic structure at resolution of 2 Å [22]. The simulations shown in Fig. 6 were done at the radiation dose of 4 $e/\text{Å}^2$, assuming a 16 bit dynamic range detector. In the reconstruction, the signal in higher-order Bragg images is focused back to the sample image by wavefront propagation. Therefore, noise superimposed onto Bragg hologram leads to noise superimposed onto the reconstructed sample distribution, as illustrated in Fig. 6(e)–(h).

For correct sampling of Bragg holograms of biological nano-crystals, a much larger number of pixels would be required for the detector, than is typically found on conventional microscopes (a detector with 2048 × 2048 pixels is used for this work). Expressed in terms of field of view and pixel sampling, if for example a 500 nm biological crystal were imaged, including Bragg images to 4th order, a field of view of 4500 nm × 4500 nm would be required. With a typical 2048 pixels per side, this would lead to a sampling of approximately 2.2 nm/pixel, which will set the resolution limit. The lateral resolution of the reconstructed structure is given by Abbe criterion: $R_{x,y} = \lambda/(2NA)$, where NA is the numerical aperture [19,23]. The simulations shown in Fig. 6 are done for a crystal of size 31.5 nm × 31.5 nm, for a total area of 400 nm × 400 nm (5 × 5 trimer units), sampled with 8000 × 8000 pixels, which gives both the pixel size and the lateral resolution according to the Abbe criterion of 50 pm. Thus, Bragg holography in principle has the potential of being a high-resolution imaging technique for biological crystals, provided that the experiments are performed employing a very large (e.g. 8000 × 8000 pixel camera [24]), shorter electron wavelength (e.g. at accelerating voltage of 20 keV) to increase the scattering angles, and small biological crystals.
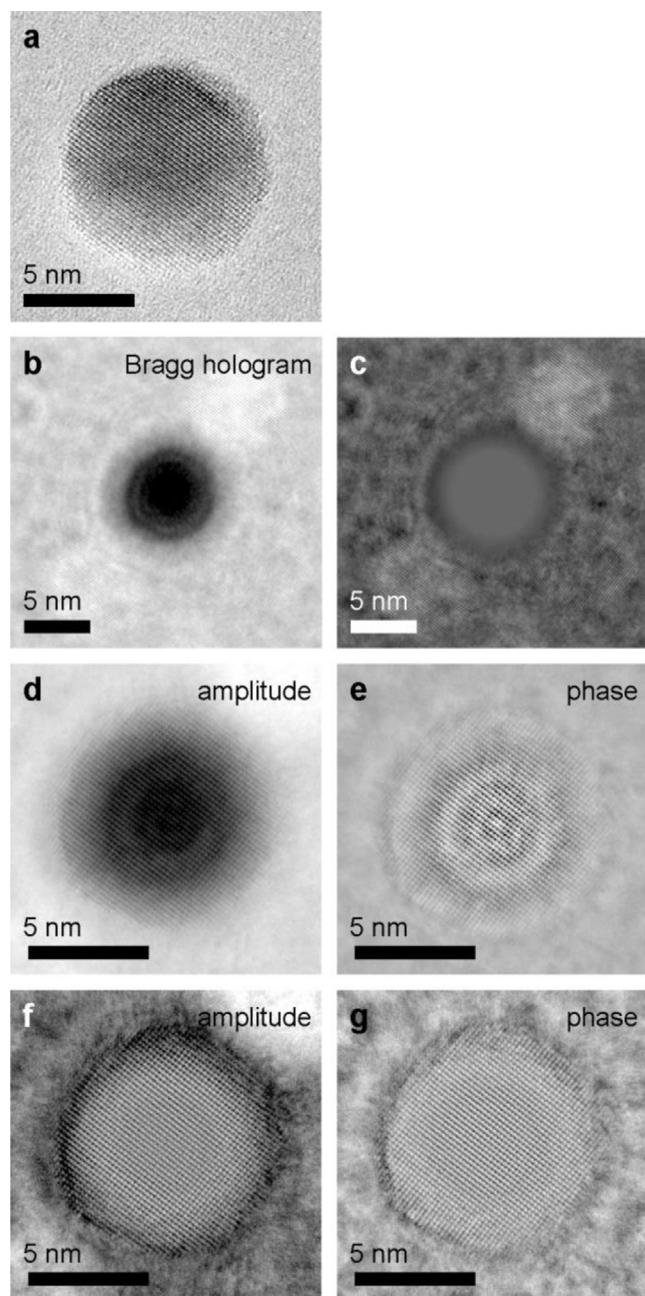
Fig. 5. Bragg holography of a Au nano-crystal realized with 300 keV electrons. (a) In-focus image of the crystal acquired in standard TEM mode. (b) Bragg hologram of the same sample obtained at defocus distance $\Delta f = 900$ nm, and the same hologram after numerical filtering (c). (d) and (e) Amplitude and phase distributions, respectively, reconstructed from the Bragg hologram by wavefront propagation to in-focus plane. Phase values in (e) are ranging from 0 to 1.50 radian. (f) and (g) Amplitude and phase distributions, reconstructed from numerically filtered Bragg hologram in which the central spot was suppressed. Phase values in (g) are ranging from 0 to 0.29 radian.

Fig. 6. Bragg holography of a bacteriorhodopsin nano-crystal, simulated study. (a) Phase distribution of the exit wave and (b) magnified region corresponding to a single trimer. The phase values are ranging from 0 to 0.71 radians. (c) Bragg hologram simulated at defocus distance $\Delta f = 10$ μm and (d) magnified region in the red square; the intensity values are $0.69 - 1.40$ au. (e) Phase distribution of the exit wave reconstructed from the Bragg hologram shown in (d) and (f) magnified region corresponding to a single trimer; the values are ranging from -0.24 to 0.65 radians. (g) and (h) the same as (e) and (f), but reconstructed from a Bragg hologram with noise added, signal-to-noise ratio SNR=10. The images are sampled with 8000 × 8000 pixels, one bacteriorhodopsin trimer is sampled with 126 × 126 pixels. The radiation dose is 4 $e/\text{Å}^2$, a 16 bit dynamic range detector is assumed in the simulations. (For interpretation of the references to color in this figure legend, the reader is referred to the web version of this article.)

3. Discussion

In conclusion, Bragg holography allows acquisition of the amplitude and phase of the wavefront scattered by a 3D nano-crystal. The crystallinity of the sample results in Bragg diffraction, the Bragg images superimposed with the reference wave provide direct access to the phase information, in one single-shot image. The recovered complete complex-valued 2D distribution of the exit wave can be propagated backward through the crystal planes, thus in principle allowing 3D atomic structure reconstruction. The reconstructed structure is not a result of averaging over the unit cells that compose the crystal, it is a direct image of the entire crystal. Crystal imperfections such as

individual defects and internal strain can be visualized. The resolution of the reconstructed nano-crystal structure is given by the NA of the imaging system. The lateral and axial (along the z axis) are given by $R_{x,y} = \lambda/(2NA)$ and $R_z = 2\lambda/(NA)^2$, respectively [19].

The experimental acquisition process is relatively robust, Bragg holograms can be conveniently acquired in a standard electron microscope. A standard scintillation-based CCD camera with relatively few pixels (2048 × 2048) was used in this work to demonstrate the concept. The full potential of the technique could be readily accessed via availability of a higher specification detector with more pixels, and higher quantum efficiency. For non-biological samples, an artifact-free (twin image free) reconstruction can be obtained by numerically suppressing the zero-order Bragg image. For this, individual Bragg images should be sufficiently separated from each other. The condition for obtaining Bragg images separated from one another is that the lateral size of the crystal s is smaller than the distance to the center of the first-order Bragg image: $s < \Delta f \tan(2\vartheta_B)$. The period of fringes in a Bragg image is given by $T = \lambda/\sin\vartheta$ where ϑ is the angle between the interfering waves, which can be re-written as $T \approx d$, where we considered the Bragg law $2d\sin\vartheta_B = \lambda n$. This period should be sampled correctly with at least two pixels per period according to the Nyquist–Shannon theorem [25,26]. For higher-order Bragg images, particularly for material science samples, this interference pattern period can be very small and when sampled incorrectly, a moiré pattern or even a constant intensity instead of the correct interference pattern may be mis-detected.

Bragg holography can be applied for high-resolution imaging of biological crystals. For biological crystals imaged with a few microns of defocus, the twin image appears as a low-frequency signal superimposed onto the reconstruction and therefore does not contaminate the high-resolution structural information. The relatively small Bragg diffraction angles due to the large lattice period in biological crystals can be compensated by using low keV energy electrons which increase scattering angles. In addition, detecting systems with a large amount of pixels should be employed to provide sufficient amount of pixels per unit cell. Overall, high-resolution real space imaging of biological crystals by Bragg holography, obtaining both amplitude and phase information, is a feasible task. While diffraction on single molecules cannot be realized due to insufficient signal from a single molecule and radiation damage problem [27], Bragg holography technique offers an alternative solution by using single molecules assembled into crystal which multiplies the scattered signal to be sufficient for detection, but at the same time allows reconstruction of individual molecules assembled into the crystal.

Declaration of competing interest

The authors declare that they have no known competing financial interests or personal relationships that could have appeared to influence the work reported in this paper.

Acknowledgments

Appendix A. Electron diffraction experiments

Electron microscopy data was acquired using a ThermoFisher Titan G2 transmission electron microscope, operated at 300 kV. This microscope is equipped a Schottky XFEG source, a spherical aberration corrector for the objective lens (CEOS Gmbh), and a 2048 × 2048 pixels Gatan Ultrascan1000XP CCD camera, with 16-bit dynamic range and 14 μm pixel size.

MgO nano-cubes were synthesized as follows. Magnesium wire (MAA0327, 1 mm diameter, Japan Fine Steel, Ltd) was ignited inside a fume hood, and the resultant smoke, containing nanocrystals, was collected on TEM grids placed above the wire. The grids were exposed to the smoke for approximately 5 s. SiN grids, with membrane thickness of 20 nm were employed (Alliance Biosystems, product number SN100-A20MP2Q05). The resultant MgO particles were consistently crystalline, with cubic external morphology, and with sizes in the range from approximately 20 to 200 nm. The specimen coverage varied with the distance between the wire and substrate, and a distance of 35 mm produced a suitable particle density on the TEM grids. The particles tended to aggregate, but nevertheless it was usually straightforward to find a single isolated particle, with no other particles within the nearby field of view.

For experiments with gold nano-crystals, commercially available gold nano-particles were utilized (Nanocomposix, Product Number AUXU10-1M, with specified diameter of 10 ± 2 nm). The suspension containing the particles (in aqueous 2 mM sodium citrate) was dropped onto copper grids with amorphous carbon support membranes.

Appendix B. Bragg hologram high-pass filtering

Transmission function of the entire area with the sample can be written as $t = 1 + o$, where one corresponds to the regions without any sample, and o is a function which describes the alternations caused in the incident wave by the presence of the sample. For example, for phase shift samples (such as biological molecules), the transmission function can be written as $t = \exp(i\sigma V_z)$, where σ is the interaction parameter and V_z is the projected potential. When illuminated by a plane wave of amplitude A, the wavefront behind the sample is given by $At = A(1+o)$ and when propagated for some distance, the wavefront becomes $A(1+o) \rightarrow A(1+O)$. The recorded intensity is $H = A^2|1+O|^2 \approx A(1 + O + O^*)$, where O is the object wavefront, O^* is the twin image wavefront, and the term $|1O|^2$ is negligibly small. Without sample, or in the regions of the hologram where the signal from the sample is negligible, the recorded intensity is given by the background: $B = A^2$, and this way the background intensity can be determined.

Bragg hologram distribution H is numerically filtered and reconstructed as follows:

(1) The average background intensity (intensity due to reference wave alone) B is evaluated from the hologram.

(2) $H2 = H/B - 1$ is calculated. This gives $H2 = H/B - 1 \approx O + O^*$.

(3) In $H2$ distribution, the central region is suppressed by setting the values to 0 with blurred edges, the obtained distribution is $H3$.

(4) o is reconstructed from O by calculating wavefront $H3$ backward to the in-focus position.

The transmission function is obtained as $t = 1 + o$ and then the absorption and phase distributions are extracted from the transmission function as explained elsewhere [28].

Appendix C. Simulation of Bragg hologram of bacteriorhodopsin

For large number of pixels, as in the present study, current computational power does not allow to perform multislice calculation [29]. Therefore, the total scattered wave here is obtained by summation over all scattered waves from individual atoms. For an individual atom at a position (x_0, y_0, z_0) the scattered wave in the far-field is given by

$$U(k_x, k_y) \approx \exp(ikz_0)\exp\left(-iz_0\sqrt{k^2 - k_x^2 - k_y^2}\right) \times$$

$$\iint \exp\left[i\sigma v_z(x - x_0, y - y_0)\right] \times$$

$$\exp\left[-i(k_x x + k_y y)\right]dxdy, \qquad (5)$$

where $v_z(x,y)$ is the projected potential of the atom. The following transformation can be applied: $FT\left(\exp\left[i\sigma v_z(x - x_0, y - y_0)\right]\right) = \exp\left[-i(k_x x_0 + k_y y_0)\right]FT\left(\exp\left[i\sigma v_z(x, y)\right]\right)$ and we an re-write Eq. (5) as

$$U(k_x, k_y) \approx \exp(ikz_0)\exp\left(-iz_0\sqrt{k^2 - k_x^2 - k_y^2}\right)\times$$

$$\exp\left[-i(k_x x_0 + k_y y_0)\right]\text{FT}\left(\exp\left[i\sigma v_z(x,y)\right]\right) =$$

$$u_i(k_x, k_y)\text{FT}\left(\exp\left[i\sigma v_z(x,y)\right]\right), \tag{6}$$

where the first term $u_i(k_x, k_y)$ depends on atomic coordinates (x_0, y_0, z_0), and the last term $\text{FT}\left(\exp\left[i\sigma v_z(x,y)\right]\right)$ is the same for all atoms of the same element type.

The atomic coordinates of bacteriorhodopsin were downloaded from protein database structure 1BRD [30,31]. The input data was an array of coordinates of all atoms (x_n, y_n, z_n) in picometers, not in pixels. Hydrogen atoms were added by using UCSF Chimera software, but their contribution was so small that they can be neglected.

The first term in Eq. (6) was calculated by summing up contributions from all atoms of the same element type:

$$u_i(k_x, k_y) = \sum_n \exp(ikz_n)\times$$

$$\exp\left(-iz_n\sqrt{k^2 - k_x^2 - k_y^2}\right)\exp\left[-i(k_x x_n + k_y y_n)\right], \tag{7}$$

where (k_x, k_y) are the coordinates in the Fourier space. No fast Fourier transforms were applied in the simulations to avoid sampling artifacts. $u_i(k_x, k_y)$ was simulated for each type of atoms separately: H, B, C, N and S, thus giving $u_H(k_x, k_y)$, $u_B(k_x, k_y)$, $u_C(k_x, k_y)$, $u_N(k_x, k_y)$ and $u_S(k_x, k_y)$.

The transmission function of a layer with an atom at $(x = 0, y = 0)$ was calculated as: $t(x, y) = \exp\left[i\sigma v_z(x, y)\right]$, where $v_z(x, y)$ is the projected potential of an individual atom calculated as:

$$v_z(r) =$$

$$4\pi^2 a_0 e \sum_{i=1}^{3} a_i K_0\left(2\pi r\sqrt{b_i}\right) +$$

$$2\pi a_0 e \sum_{i=1}^{3} \frac{c_i}{d_i}\exp\left(-\frac{\pi^2 r^2}{d_i}\right)$$

where $r = \sqrt{x^2 + y^2}$, a_0 is the Bohr' radius, e is the elementary charge, $K_0(\ldots)$ is the modified Bessel function and a_i, b_i, c_i, d_i are parameters that depend on the element type of the atoms and are tabulated in Ref. [29]. In $v_z(r)$, the singularity at $r = 0$ was replaced by the value of $v_z(r)$ at $r = 0.1$ Å. The transmission function is simulated for each type of atoms separately: H, B, C, N and S, thus giving $t_H(x, y)$, $t_B(x, y)$, $t_C(x, y)$, $t_N(x, y)$ and $t_S(x, y)$. The total wavefront in the far-field was calculated according to Eq. (7) as a sum of the products of the Fourier transform of the scattered wave with atomic coordinates over all chemical elements:

$$\sum_{i=H,B\ldots} \text{FT}\left[t_i(x, y) - 1\right] U_i(k_x, k_y), \tag{8}$$

where $U_i(k_x, k_y)$ is a sum over all $u_i(k_x, k_y)$ for all atoms of particular element type. In Eq. (8), one is subtracted to avoid summing up of the unscattered wave for all atoms. The exit wave is then obtained by inverse Fast Fourier transform (FFT) of the result of Eq. (8) and adding one (unscattered wave).

References

[1] M. Ladd, R. Palmer, Structure Determination By X-Ray Crystallography, Springer, 2013.

[2] Y.S. Yang, et al., Deciphering chemical order/disorder and material properties at the single-atom level, Nature 542 (2017) 75–79.

[3] M. Gemmi, E. Mugnaioli, T.E. Gorelik, U. Kolb, L. Palatinus, P. Boullay, S. Hovmoller, J.P. Abrahams, 3D electron diffraction: the nanocrystallography revolution, ACS Central Sci. 5 (2019) 1315–1329.

[4] B.L. Nannenga, T. Gonen, The cryo-EM method microcrystal electron diffraction (MicroED), Nature Methods 16 (2019) 369–379.

[5] M.G. Rossmann, R. Henderson, Phasing electron-diffraction amplitudes with the molecular replacement method, Acta Crystallogr. Sect. A 38 (1982) 13–20.

[6] W. Coene, G. Janssen, M.O. Debeeck, D. Vandyck, Phase retrieval through focus variation for ultra-resolution in field-emission transmission electron microscopy, Phys. Rev. Lett. (1992) 3743–3746.

[7] J. Miao, P. Charalambous, J. Kirz, D. Sayre, Extending the methodology of X-ray crystallography to allow imaging of micrometer-sized non-crystalline specimens, Nature 400 (1999) 342–344.

[8] J.M. Zuo, I. Vartanyants, M. Gao, R. Zhang, L.A. Nagahara, Atomic resolution imaging of a carbon nanotube from diffraction intensities, Science 300 (2003) 1419–1421.

[9] L.D. Caro, E. Carlino, G. Caputo, P.D. Cozzoli, C. Giannini, Electron diffractive imaging of oxygen atoms in nanocrystals at sub-angstrom resolution, Nat. Nantiechnol. 5 (2010) 360–365.

[10] L.D. Caro, E. Carlino, F.A. Vittoria, D. Siliqi, C. Giannini, Keyhole electron diffractive imaging (KEDI), Acta Crystallogr. A 68 (2012) 687–702.

[11] J.S. Wu, U. Weierstall, J.C.H. Spence, RETRACTED: Diffractive electron imaging of nanoparticles on a substrate (Retracted Article. See vol 5, pg 837, 2006), Nature Mater. 4 (2005) 912–916.

[12] C.J. Russo, R. Henderson, Ewald sphere correction using a single side-band image processing algorithm, Ultramicroscopy 187 (2018) 26–33.

[13] D. Gabor, A new microscopic principle, Nature 161 (1948) 777–778.

[14] D. Gabor, Microscopy by reconstructed wave-fronts, Proc. R. Soc. Lond. Ser. A Math. Phys. Eng. Sci. 1051 (1949) 454–487.

[15] T. Latychevskaia, H.-W. Fink, Solution to the twin image in holography, Phys. Rev. Lett. 98 (2007) 233901.

[16] J.A. Ratcliffe, Some aspects of diffraction theory and their application to the ionosphere, Rep. Progr. Phys. 19 (1956) 188–267.

[17] J.W. Goodman, Introduction To Fourier Optics, third ed., Roberts & Company Publishers, 2004.

[18] T. Latychevskaia, H.-W. Fink, Practical algorithms for simulation and reconstruction of digital in-line holograms, Appl. Opt. 54 (2015) 2424–2434.

[19] T. Latychevskaia, Lateral and axial resolution criteria in incoherent and coherent optics and holography, near- and far-field regimes, Appl. Opt. 58 (2019) 3597–3603.

[20] T. Latychevskaia, Three-dimensional structure from single two-dimensional diffraction intensity measurement, Phys. Rev. Lett. 127 (2021) 063601.

[21] B. Thompson, Fraunhofer holography, Proc. SPIE 67 (1968) 0015.

[22] R. Henderson, Realizing the potential of electron cryo-microscopy, Q. Rev. Biophys. 37 (2004) 3–13.

[23] E. Abbe, The relation of aperture and power in the microscope, J. Royal Micr. Soc. 2 (1882) 300–309.

[24] H. Adaniya, M. Cheung, C. Cassidy, M. Yamashita, T. Shintake, Development of a SEM-based low-energy in-line electron holography microscope for individual particle imaging, Ultramicroscopy 188 (2018) 31–40.

[25] V.A. Kotelnikov, On the transmission capacity of the ether and wire in electrocommunications, Izd. Red. Upr. Svyazzi RKKA (1933).

[26] C.E. Shannon, Communication in the presence of noise, Proc. IEEE 86 (1949) 447–457.

[27] R. Neutze, R. Wouts, D. van der Spoel, E. Weckert, J. Hajdu, Potential for biomolecular imaging with femtosecond X-ray pulses, Nature 406 (2000) 752–757.

[28] T. Latychevskaia, H.-W. Fink, Simultaneous reconstruction of phase and amplitude contrast from a single holographic record, Opt. Express 17 (2009) 10697–10705.

[29] E.J. Kirkland, Advanced Computing in Electron Microscopy, Springer, 2010.

[30] R. Henderson, J.M. Baldwin, T.A. Ceskaa, F. Zemlin, E. Beckmann, K.H. Downing, Model for the structure of bacteriorhodopsin based on high-resolution electron cryo-microscopy, J. Mol. Biol. 213 (1990) 899–929.

[31] R. Henderson, J.M. Baldwin, T.A. Ceskaa, F. Zemlin, E. Beckmann, K.H. Downing, ID: 1BRD, PDB, 1990, p. 10.2210/pdb2211BRD/pdb.